Innovative Robotics for Liquid Environs: MRI Gauss Guns and Drift Nodes

by Jarrett Lane Lonsford

A thesis submitted to the Department of Mechanical Engineering in partial fulfillment of the requirement for the degree of

Master of Science

in Aerospace Engineering

Chair of Committee: Dr. Karolos Grigoriadus

Co-Chair of Committee: Dr. Aaron T. Becker

Committee Member: Dr. Matthew Franchek

Committee Member: Dr. Craig Glennie

University of Houston

December 2019

Acknowledgements

This material is based upon work supported by the National Science Foundation under Grant No. CNS-1646566, CNS-1646607, and IIS-1553063. Any opinions, findings, and conclusions or recommendations expressed in this material are those of the authors and do not necessarily reflect the views of the National Science Foundation.

Abstract

This thesis covers the following two projects: MRI Compatible Gauss Guns (sections I-VI) and Biodegradable Drift Nodes (VII-XI).

Project 1: Millirobots propelled and imaged by MRI are a promising approach for minimally invasive therapies. The strong constant magnetic field inside the MRI precludes torque-based control. Consequently, prior propulsion techniques have been limited to gradient-based pulling through fluid-filled body lumens using the weaker magnetic gradient coils. One mechanism to generate additional force to pierce tissue is an MRI Gauss gun, a device that stores magnetic potential energy in an internal arrangement of components. This potential energy can be released through a self-assembly operation. This report presents a new design for an underwater MRI Gauss gun with numerical analysis and results for optimizing the kinetic energy generated. Experiments performed both inside and outside the MRI, in air and underwater validate the optimization analysis.

Project 2: As Earth faces environmental changes such as rising sea levels, melting ice caps and increasingly severe tropical storm systems, monitoring of our oceans has become increasingly important. Many of the oceanic environments that require monitoring are vast and dangerous, making the successful deployment and subsequent retrieval of these devices challenging. Ideally, monitoring devices for harsh climates would not require retrieval if they are inexpensive, environmentally benign, and fully degradable. This report describes the design, fabrication and testing of a network of cheap monitoring devices known as Drift Nodes and the ongoing process to make them fully biodegradable, from the 3d-printed housing to the electronics, sensors and batteries.

Table of Contents

List of Tables

List of Figures

I. Gauss Gun Introduction and Related Work

Sections I-VI present work from “Numerical Optimization, Design, and Testing of an Underwater-Firing Self-Assembled Gauss Gun” by Mohammad M. Sultan, Jarrett Lonsford, Javier Garcia, Julien Leclerc, Mohamad Ghosn and Aaron T. Becker, under preparation. My contributions for this project include the design and fabrication of several iterations of Gauss guns that can assemble and fire underwater, conducting optimization experiments and MRI experiments, and processing collected data.

Catheter-based surgeries, which insert surgical tools through body lumens using a long tube, were introduced in 1964 [1]. It is hard to overstate the value of catheter-based interventions as a surgical tool. Indeed, an estimated 955,000 coronary angioplasties were performed in the US in 2010 [2]. However, catheter-based interventions have several drawbacks: they require a long trailing catheter that can dislodge plaques, distend vessels, and reduces the amount of surgical force at the distal tip. As an alternative, this paper investigates a type of milli-robot that can travel tetherless through body lumens, self-assemble into a more powerful tool, and discharge a surgically relevant amount of force. This builds on recent work using magnetic gradients to navigate through the natural fluid-filled passageways of the body, such as the circulatory system or cerebrospinal fluid spaces. While navigation is sufficient for some applications, it can also be necessary to penetrate the surrounding tissue. Potential applications include puncturing a membrane to release trapped fluid, opening a blocked passageway, brachytherapy, or delivering a drug to a tissue location several centimeters from a fluid-filled space.

The forces required for tissue penetration are substantially higher than those needed to propel a milli-robot through a bodily fluid and consequently can be difficult to achieve. Prior tetherless systems for moving through tissue have relied on magnetic forces and torques produced by large external magnets to either pull magnetic spheres through brain tissue [3] or to rotate threaded magnetic cylinders through muscle tissue [4]. Alternatively, methods for tetherless robot propulsion and control have been developed that employ the magnetic gradients of clinical MRI scanners [5]–[8]. MRI-based milli-robot navigation in the vasculature was first demonstrated in [5]. MRI also provides the capability to image both the robot and surrounding tissue to guide navigation. However, these techniques constrain the motion of MRI-powered spheres to fluid-filled spaces since the magnetic gradients produced by the scanner are relatively weak and is not capable of producing tissue penetration. The maximum gradient produced by most clinical scanners is in the range of $20\text{-}40\ mT/m$ producing a force on a magnetized steel particle equal to $36\text{-}71\%$ of the gravitational force. It is possible to install custom high-strength gradient coils, such as $400\ mT/m$ coil reported in [9], but this approach is costly and can reduce the size of the MRI bore. Design can reduce the force required for penetration. A standard 18-gauge needle requires $0.59\text{-}0.11\ N$ of force to penetrate $10\ mm$ into muscle tissue. Bio-inspired design can somewhat reduce these forces, e.g., the backward-tipped barbs of the North American porcupine quill exhibit forces of $0.33\text{-}0.08\ N$ for $10\ mm$ of muscle penetration [10]. Nevertheless, to reproduce even these forces using an MRI with a steel needle would require a 3.3 m long shaft, since gradient force is proportional to the volume of ferromagnetic material. Such a length is longer than the bore of the scanner. While the size of macro-scale MRI-based actuators permits the use of gear transmissions to trade off velocity and force [6], [11], this approach is not feasible at the millimeter scale. Therefore, to address the challenge of MRI-based tissue penetration, an alternative to gradient-based force production is needed.

Tissue puncture force is inversely related to penetration velocity [12], which motivates the concept of using energy storage and sudden release to perform penetration. Furthermore, while the maximum gradient forces produced on a steel particle are low, the magnetic attraction forces between particles inside the scanner is, by comparison, quite high. Thus, the approach proposed here involves navigating individual spheres to a target location and allowing them to self-assemble in a manner that focuses the stored magnetic potential energy as kinetic energy for tissue penetration. The concept, illustrated in Figure 1, corresponds to a Gauss gun [13], [14].

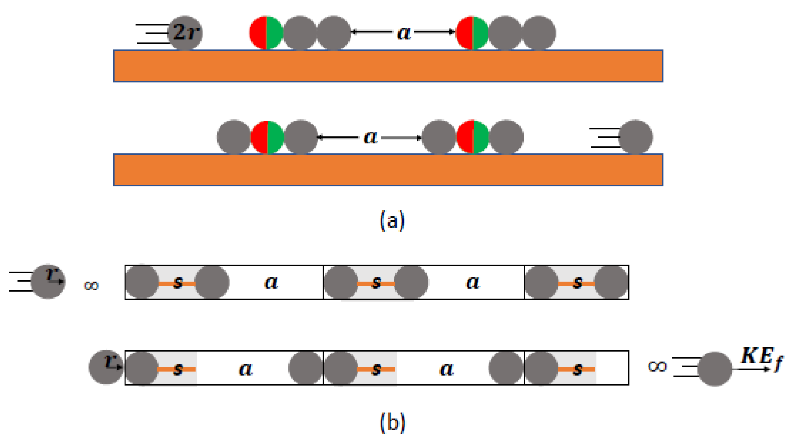

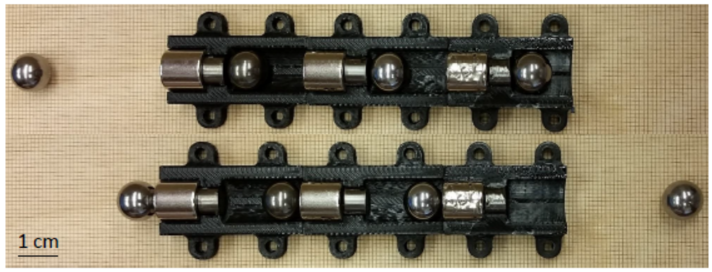

(c)

(d)

Fig. 1. Operation of a Gauss gun. (a) Standard design for use outside an MRI scanner shown before and after triggering. Magnetized spheres are red and green. Non-magnetized spheres are gray. (b) Design for use inside an MRI shown before and after triggering. All spheres (r = 4.75mm) are magnetized when inside scanner. (c) MRI Gauss gun and (d) small scale Gauss gun (r = 1.59mm) implemented inside the lab.

Comprised of one or more stages, each stage is composed of a strong magnet, followed by two or more steel spheres (bearing balls). By colliding a single steel sphere with the first magnet, a chain reaction is initiated, greatly amplifying the speed of the first sphere. In an MRI scanner there is no need for permanent magnets, since steel is highly magnetized by the magnetic field of an MRI. Each stage contains two magnetized spheres separated by a nonmagnetic spacer and held together by magnetic forces. Using existing control approaches [6], [8], stages can be navigated through fluid-filled spaces and self-assembled at a desired penetration location. The assembly can then be fired by a single sphere. This research is an expansion of a preliminary conference paper that introduced the concept of an MRI Gauss gun [15]. The new contributions include numerical optimization, a design that can now fire underwater, high speed motion analysis, and submerged tests in an MRI. Locations with geometries favorable for Gauss gun assembly include the bladder and the coronary artery, as shown in Figure 2.

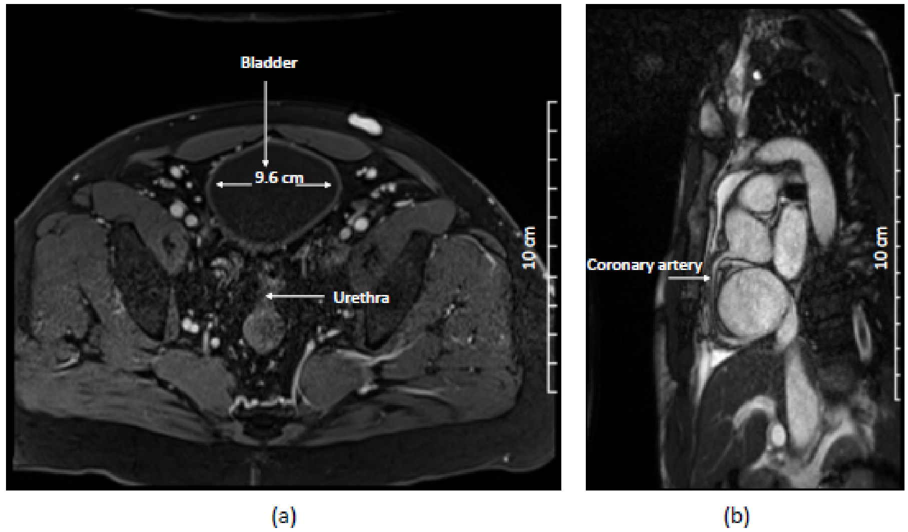

Fig. 2. MRI images of the (a) bladder and urinary system and (b) coronary arteries.

Section II explains the force, the torque and the energy inside an MRI Gauss gun, as well as the design and the materials used. Section IV discusses numerical, analytical and study cases for the MRI Gauss gun. Section V presents experiments performed both inside and outside MRI in air and underwater. Section VI concludes with an overview of the results and suggestions for future work.

II. MRI Gauss Gun Theory

This section builds a model of an MRI Gauss gun. It starts with a dipole force and torque model, then an overview of the structure of a Gauss gun and finishes with a model on how a Gauss gun converts magnetic potential energy into kinetic energy.

A. Magnet Force Calculation inside MRI

Any ferrous material placed in the magnetic field of an MRI scanner becomes a strong magnetic dipole. The gradient fields can then apply forces on these dipoles. Additionally, the dipoles exert forces on each other. Dipole forces overpower MRI gradient forces if the materials are closer than a threshold distance. The magnetic field at position p_2 generated by a spherical magnet at position p_1 with magnetization m_1 is [16]

$$B_{p_1}(p_2) = \frac{\mu_0}{4\pi}\frac{3n_{12}(n_{12}\cdot m_1)-m_1}{|p_2-p_1|^3}, \tag{1}$$

with $n_{12} = (p_2 - p_1)/|p_2 - p_1|$. This is the magnetic field of a dipole. The force applied to a dipole at p_1 with magnetic moment m_1 by another dipole at p_2 with magnetic moment m_2 is approximated by

$$F_{12} \approx \frac{3\mu_0}{4\pi}\frac{1}{|p_2-p_1|^4}\begin{bmatrix} 5n_{12}\big((m_1\cdot n_{12})(m_2\cdot n_{12})\big) - n_{12}(m_2\cdot m_1) \\ -m_1(m_2\cdot n_{12}) - m_2(m_1\cdot n_{12}) \end{bmatrix}. \tag{2}$$

The torque applied on a dipole p_2 at by a dipole at p_1 is

$$\emptyset_{12} = m_2 \times B_{p_1}(p_2). \tag{3}$$

Inside a 3T MRI, a steel sphere becomes fully magnetized with magnetic saturation $M_s = 1.36 \times 10^6$. The magnetic moment of a sphere with radius r_{sphere} is aligned with the MRI B_0 field:

$$m(r_{sphere}) = [0\ 0\ 1]\frac{4}{3}\pi r_{sphere}^3 M_s. \tag{4}$$

Figure 3 shows contour plots for the magnetic force exerted by two identical spheres on each other.

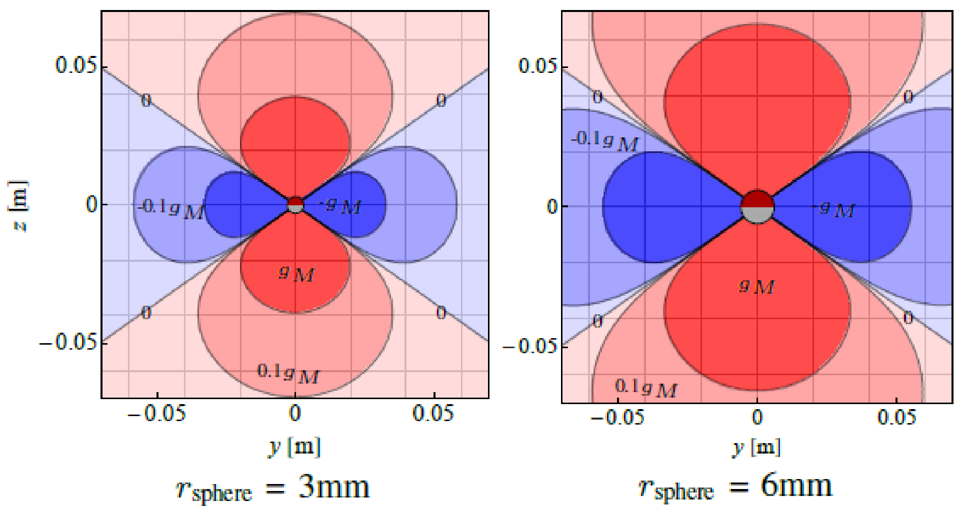

Fig. 3. Contour lines show the force component radially outward from a sphere at (0; 0) on an identical sphere in an MRI. The magnetic field is symmetric about the z-axis. Contour lines at the maximum gradient field of the MRI, g_M, are shown for comparison.

The contour lines show $F \cdot n_{12}$, the force component radially outward from the sphere at (0; 0) compared to the maximum force provided by the gradient coils g_M. This force is attractive (red) along the z-axis and repulsive (blue) perpendicular to z. The magnetic field is symmetric about the z-axis. If two spheres move within the dark red region, they cannot be separated using the gradient field. The contour lines are drawn at $F_{12} \cdot n_{12} = g_M \cdot \left\{-1, -\frac{1}{10}, 0, \frac{1}{10}, 1\right\}$. The maximum force is along the z-axis

$$F_{attraction} = -\frac{8M_s^2\mu_0\pi r_1^3 r_2^3}{3d^4}, \tag{5}$$

where d is the distance separating two spheres of radii r_1 and r_2, each with magnetic saturation M_s. The vacuum permeability μ_0 is, by definition, $4\pi \times 10^{-7}\ V \cdot s/(A \cdot m)$. The critical distance when the attractive force becomes greater than the maximum gradient force is

$$\sqrt[4]{\frac{2M_s\mu_0 r_{sphere}^3}{g_M}}. \tag{6}$$

B. Magnetic Torque on MRI Gauss Gun

Because each Gauss gun component has at least two ferrous spheres, the MRI B_0 field creates a torque that acts to align the components parallel to the z-axis. Applying (3), with magnetic moments given by (4), on a component with sphere radii r_1 and r_2, separated by distance between centers, and the line between the spheres at an angle of θ from z, generates the restoring torque

$$\tau = \frac{4}{3s^3} M_s^2 \pi\mu_0 r_1^3 r_2^3 s\ n(2\theta). \tag{7}$$

Both decreasing s and increasing r_1 and/or r_2 increases this torque. This torque results in stable equilibrium configurations pointing along the ±z-axis and unstable equilibriums perpendicular to the axis. The stable equilibriums correspond with maximum attractive force between the spheres, and the unstable equilibriums with maximum repulsive force.

C. MRI Gauss Gun Design

An MRI Gauss gun can use ferromagnetic components instead of permanent magnets and requires non-magnetic spacers between magnetic components. The MRI Gauss gun can have three types of components: The *trigger component* fires the Gauss gun by starting a chain reaction. Part (a) in Figure 4 represents the trigger component, in this instance the trigger is a simple magnetic sphere.

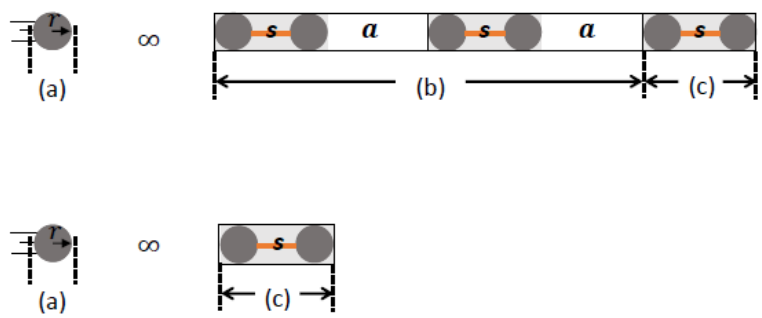

Fig. 4. The top part shows three–stage MRI Gauss gun with all the components, (a) Trigger component, (b) Barrel component contains two stages and (c) Delivery component, while the bottom part shows one-stage MRI Gauss gun contains only the (a) Trigger component and (c) Delivery component.

The *barrel component* (optional) is the middle stage(s) between the firing and delivery components, labelled (b) in Figure 4. Each barrel component has two spheres separated by a non-magnetic spacer of length s between the spheres followed by an air gap with length a. To prevent the assembled Gauss gun from accidentally triggering, a must be greater than s. The barrel component is used to achieve stronger forces because each stage stores potential energy. The bottom part in Figure 4 shows a Gauss gun without a barrel component.

The *delivery component* is the final stage, labelled Part (c) in Figure 4. It contains two magnetic components separated by a non-magnetic spacer s. The distal magnetic component is fired into tissue and should be designed for the desired task. For example, the distal component can be functionalized to deliver a drug, shaped to cut tissue, or could be a brachytherapy seed containing a magnetic component. The number of MRI Gauss gun stage(s), N, is the number of barrel components plus the delivery component.

D. MRI Gauss Gun Energy Conversion

This section investigates MRI compatible Gauss guns. An MRI Gauss gun has N stages. In the default design each component has two spheres of radius r separated by a nonmagnetic spacer with length s. After each barrel component is an air gap of length a. Without the trigger component, the system is stable. Each stage has potential energy PE_{MB}, which is the energy required to release a sphere from the stage and is calculated in the following section.

1) Magnetic Potential and Kinetic Energy: The calculations in this section ignores heat, friction, and mechanical losses. Because magnetic forces decay with an inverse cubic relationship, analysis is simplified by only considering forces between adjacent spheres. To calculate the energy required to release a sphere from its stage, integrate $F_{attraction}$ in (5)

$$PE_{MB} = -\int_{d}^{\infty} -\frac{8M_s^2\mu_0\pi r_1^3 r_2^3}{3d^4}\,dx \tag{8}$$

$$\text{and } PE_{MB} = -\frac{C}{(2r+s)^3}. \tag{9}$$

KE_{∞} is the kinetic energy that the trigger sphere gains by the attraction force exerted while it approaches the first stage (step b in Figure 5).

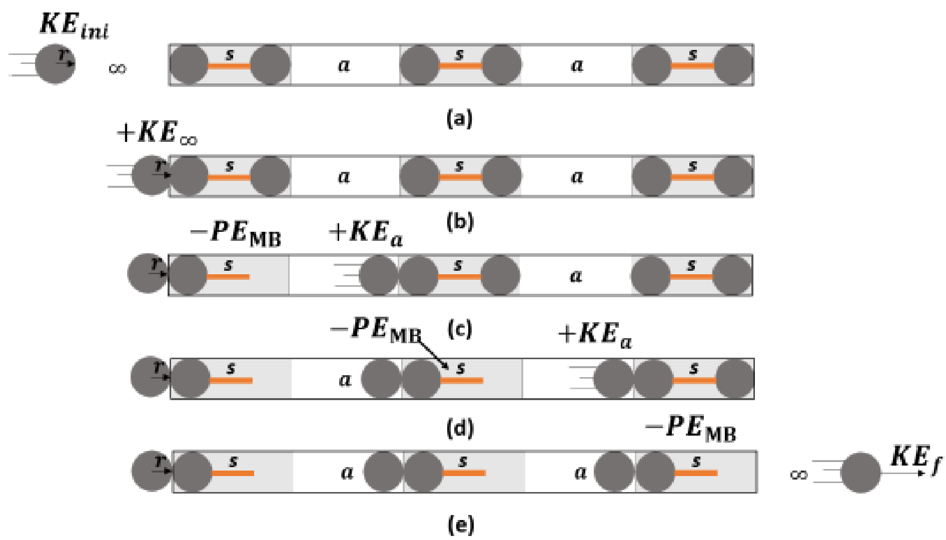

Fig. 5. Illustration of component rearrangement in a three stage MRI Gauss gun. (a) The trigger component moves with KE_∞ initial to the first stage from the MRI Gauss gun, (b) Trigger component hits first sphere with energy KE_∞, (c) Sphere 3 hits sphere 4 with energy $KE_\infty - PE_{MB} + KE_a$, (d) Sphere 5 hits sphere 6 with energy $KE_\infty - 2PE_{MB} + 2KE_a$ and (e) The delivery projectile moves with energy $KE_\infty - 3PE_{MB} + 2KE_a$.

This kinetic energy is calculated as

$$KE = -\Delta PE \tag{10}$$

$$\text{and } \Delta PE = -\int_{ref}^{r} F_{attraction}\, dx. \tag{11}$$

Substituting (5) and (10) into (11) results in

$$KE_\infty = -\int_{\infty}^{2r} \frac{8M_s^2\mu_0\pi r_1^3 r_2^3}{3x^4}\, dx = \frac{C}{(2r)^3}. \tag{12}$$

Here $C = \frac{8}{9}M_s^2\mu_0\pi r_1^3 r_2^3$ includes all terms except the distance between the spheres. KE_a is the kinetic energy the sphere released by the previous stage gains by the attraction force exerted by the current stage (step c and d in Figure 5). Using equations (5), (10), and (11)

$$KE_a = -\int_{a+2r}^{2r} \frac{8M_s^2\mu_0\pi r_1^3 r_2^3}{3x^4} dx, \tag{13}$$

$$KE_a = \frac{8M_s^2\mu_0\pi r_1^3 r_2^3}{9(2r)^3} - \frac{8M_s^2\mu_0\pi r_1^3 r_2^3}{9(2r+a)^3}, \tag{14}$$

and $$KE_a = C\left[\frac{1}{(2r)^3} - \frac{1}{(2r+a)^3}\right]. \tag{15}$$

2) Energy System Mechanism and Final Kinetic Energy: Before firing, the barrel and delivery components are stable because there is a restoring force that returns any sphere to initial configuration if a small displacement is applied. As shown in Figure 5 (a), each stage in these components has potential energy PEMB. PEMB is the energy needed to break the magnetic bond and release a sphere to the next stage. The system has energy losses equal to the number of stages times the potential energy:

$$E_{Losses} = (N)PE_{MB}. \tag{16}$$

After firing, the trigger sphere hits the first sphere of the first stage as shown in Figure 5(b). In this impact between the trigger component and the barrel component, KE_∞ transfers to the first stage. If KE_∞ is greater than PE_{MB}, this breaks the magnetic bond in the first stage and releases the second sphere from the first stage with energy equal to $KE_\infty - PE_{MB}$ as shown in Figure 5 (c). Once sufficiently displaced from its stable resting position, the released sphere is propelled by attractive forces toward the first sphere in the second stage. The released sphere gains KE_a J of energy. The net energy gain will transfer to the next stage as in Figure 5(d). This process repeats until the sphere delivered to the last stage releases the projectile, which gains kinetic energy KE_f as in (19):

$$KE_f = KE_\infty + (N-1)KE_a - (N)PE_{MB}, \tag{17}$$

$$KE_f = \frac{C}{(2r)^3} + (N-1)C\left[\frac{1}{(2r)^3} - \frac{1}{(2r+a)^3}\right] - (N)\frac{C}{(2r+s)^3}, \tag{18}$$

and $$KE_f = (N)\frac{C}{(2r)^3} - (N-1)C\frac{1}{(2r+a)^3} - (N)\frac{C}{(2r+s)^3}. \tag{19}$$

If $N = 1$, there is no barrel component and the final kinetic energy simplifies to:

$$KE_f = \frac{C}{(2r)^3} - \frac{C}{(2r+s)^3}. \tag{20}$$

III. Gauss Gun Shape Optimization

The previous section assumed that the magnetic components are infinitely small and approximated them as magnetic moments. This assumption is valid when the interacting components are sufficiently far from each other. This section studies the interaction of the magnetic components at distances inferior to $10\ mm$.

Finite elements simulations were performed using the software Finite Element Method Magnetics (FEMM, [17]). The system was modeled using a 2D axisymmetric geometry. For each simulation two magnetic components were placed inside the domain to solve. A constant and uniform magnetic field $H_{app} = 3.18$ MA/m oriented along the revolution axis was applied in the complete domain by setting the boundary conditions. This magnetic field value corresponds to the field produced by a $3\ T$ MRI scanner.

The simulations were performed for distances between the magnetic components ranging from 0 to $10\ mm$. Three different shapes for the magnetic components were tested: spherical, cylindrical and a cylindrical with a conical tip. All the simulated components have the same volume ($452.6\ mm^3$) and the same diameter ($9.52\ mm$). The material used for the simulations is 1006 steel. The non-linear magnetic behavior of this material was considered during the simulations. Figure 6 shows the geometry of these components and the calculated flux density maps obtained when the components are placed at distance of $1\ mm$ from each other.

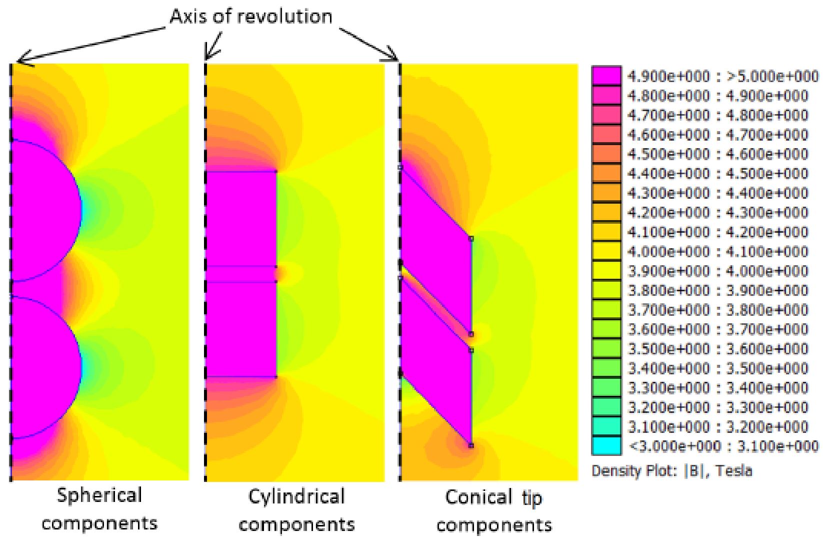

Fig. 6. Flux density map computed for different magnetic elements geometry. In each case, the magnets have a radius of 9.52 mm and are separated by 1 mm.

The applied flux density is equal to 3 T, however, the flux density is higher inside the ferromagnetic material and lower on its radial side. The magnetization of the material indeed produces an additional magnetic field H_d. This field is oriented in the same direction as the applied field inside the material which explain the flux density increase. H_d propagates outside of the material and, on the radial side, it is opposed to H_{app} which produces a decrease of the total magnetic field, an effect also called demagnetization [18]. Figure 7 shows a plot of the force resulting from the magnetic interaction between two magnetic components as a function of the distance separating them.

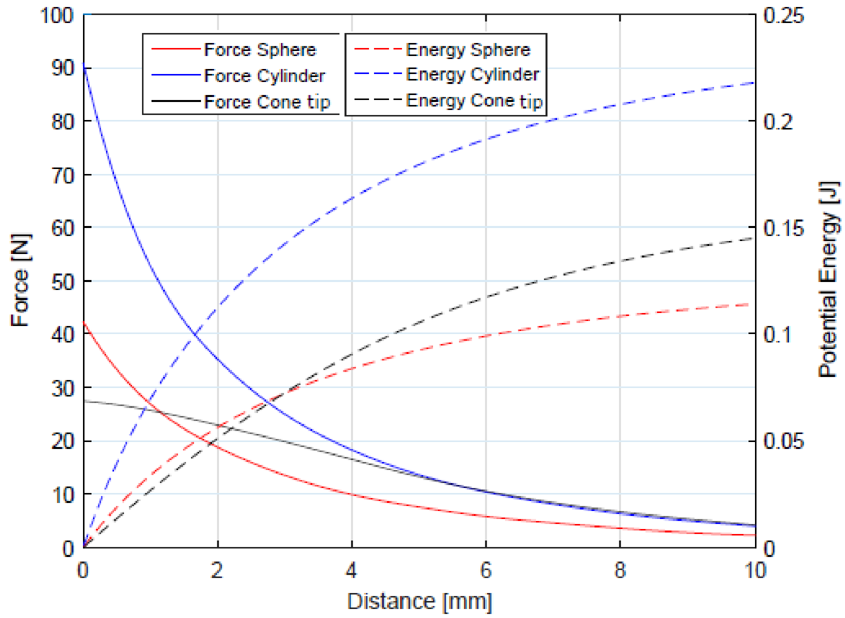

Fig. 7. Force resulting from the magnetic interaction between two magnetic components as a function of the distance separating them. The corresponding potential energy is also shown.

The corresponding potential energy is also shown. Cylindrical magnetic components possess the highest potential energy of the simulated shapes and are therefore expected to produce the highest velocities. The force produced using spherical components is 40 to 55 % lower depending on the distance. The force produced by the components with conical tip is the lowest for distances inferior to 1.15 mm. It is slightly higher than the force produced by the sphere on the rest of the curve and the potential energy is slightly larger than that of the sphere when the distance is superior to $3mm$. This analysis indicates that spheres are not the optimal shape for storing potential energy, however they are efficient for transferring energy and momentum, and are used throughout the rest of this work.

IV. Analytical and Numerical Optimization

A. MRI Gauss Gun Constraints

The medical procedure and dimensions of the human patient provides several constraints on the size of the assembled Gauss gun and the length and radius of individual components. Assume that the assembled MRI Gauss gun's total length must be less than or equal to L, in which L includes all the components of the Gauss gun as shown in Figure 5. For an N stage Gauss gun with equal-size spheres, and constant length air gaps and spacers, L is

$$L = 2(2N + 1)r + Ns + (N - 1)a. \tag{21}$$

This L is the first constraint. The second constraint is that the air gap a between any two stages must be greater than the spacer s between any two spheres inside each stage. This constraint on a provides a stability margin that prevents the MRI Gauss gun from premature firing. As shown in (21), for every N value L is a linear function of r, s, and a. This property enables us to nondimensionalize the optimization, giving design guidelines for any size of MRI Gauss gun.

B. Analysis and Results

This section describes a technique that maximizes KE as in (19) for two cases and different N values:

- Case 1: all spheres have the same radii for $N = 1$ through 10.

- Case 2: spheres may have different radii for $N = 1$ and $N = 2$.

All optimization was conducted in Mathematica using the Nelder Mead method.

1) Numerical analysis when all spheres have the same radii: We start by maximizing KE with the constraint that all spheres have the same radius because they are low cost and available off the shelf, high-accuracy identical spheres. Figure 8 represents the plot KE/L^3 vs. r/L for N from 1 to 10.

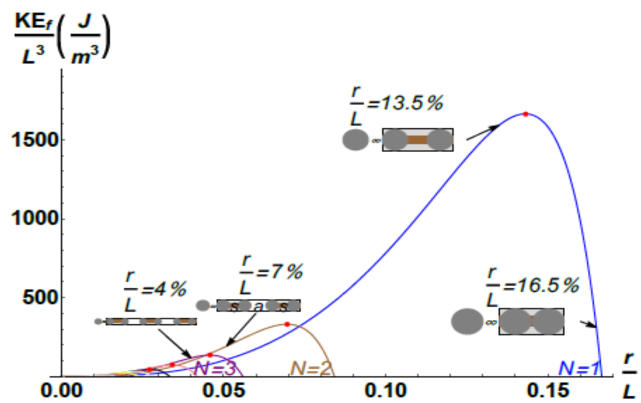

Fig. 8. maximum KE/L^3 vs. r/L for Gauss guns with equal radii spheres for $N \in [1;\ 10]$. Each curve represents a stage.

In this plot, there are ten curves. Each curve represents the number of stages the MRI Gauss gun has starting from one-stage to ten stages. The red point on each curve represents the optimum KE value for each curve. This plot has nondimensionalized axes, which can be used for any L value. For instance, if $KE/L3$ at $r/L = 0.143$ when $N = 1$ is $1664.6\ J/m3$, thus for $L = 10\ mm$, the optimal r is $1.43\ mm$ and KE is $166.46\ mJ$. Results for each curve can be found in Table 1 below and an example of maximum KE gauss guns for each curve is shown in Figure 9.

Table I: Max Kinetic Energy Released for N-Stage Gauss Guns with Equal-Radii Spheres

N	r/L	s/L	a/L	KE/L^3
1	0.143	0.142	0	1664.6
2	0.07	0.078	0.148	331.5
3	0.046	0.053	0.099	135.7
4	0.034	0.041	0.074	73.2
5	0.027	0.032	0.06	45.6
6	0.023	0.027	0.0499	31.1
7	0.019	0.023	0.043	22.6
8	0.017	0.021	0.037	17.1
9	0.015	0.018	0.033	13.4
10	0.013	0.017	0.03	10.8

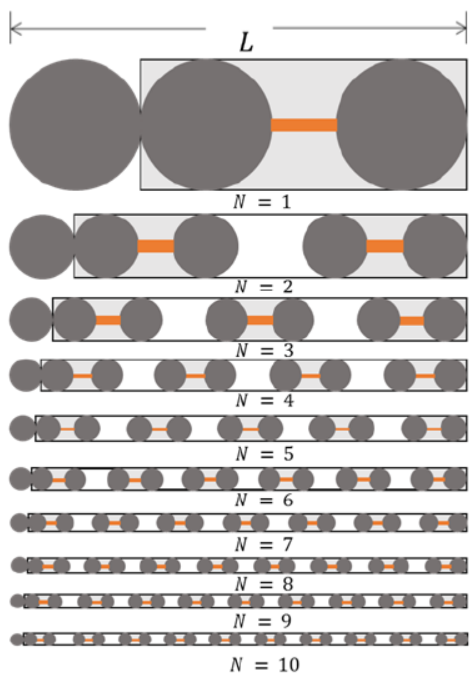

Fig. 9. Maximum KE Gauss guns with the same length L and equal radii spheres for $N \in [1;\ 10]$.

2) Numerical analysis using different radii when $N = 1$ and $N = 2$: This section reports numerical optimization after relaxing the constraint that all sphere radii are equal. This enables generating larger kinetic energy at the expense of more computation. Figure

10 shows contour plots of nondimensionalized energy (J/m^3) for one-stage Gauss guns with different radii.

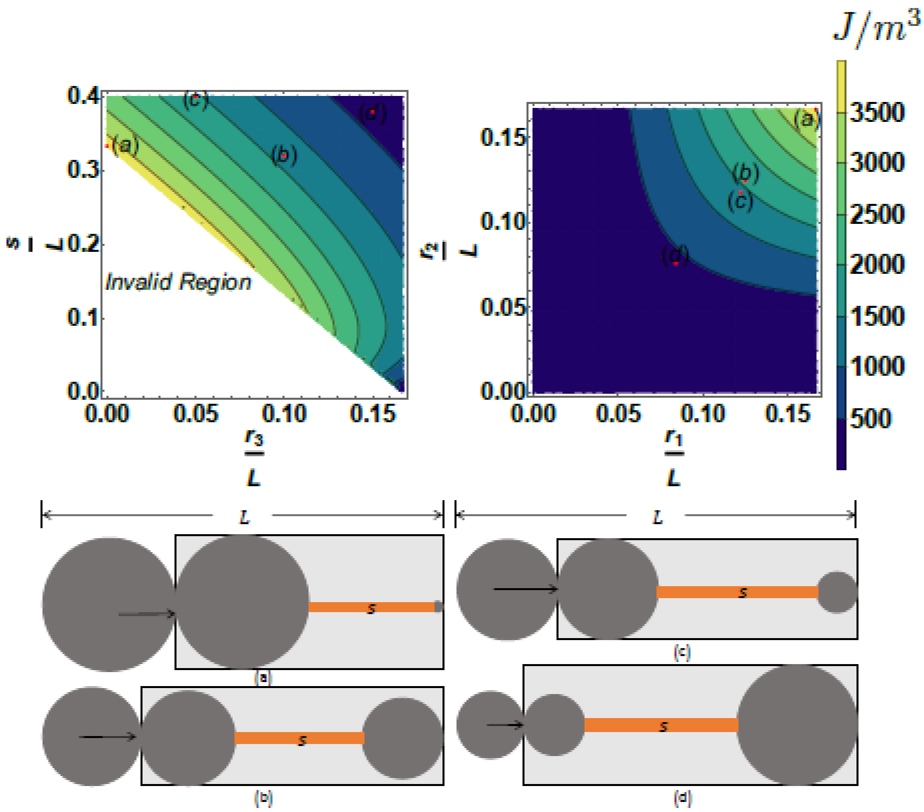

Fig. 10. Contour plot for r_1/L vs. r_2/L and r_3/L vs. s/L. Four representative one-stage MRI Gauss guns are illustrated by red points.

Each contour plot holds two parameters constant and varies two parameters. The parameters are the spacer length s between the second and the third spheres and the three sphere radii r_1; r_2; and r_3. Four representative Gauss gun designs with parameter values given in Table II are shown and drawn as red points in Figure 10.

Table II: Four One-Stage Gauss Guns, Shown as Red Points in Figure 10

point	r_1/L	r_2/L	r_3/L	s/L	KE/L^3
(a)	0.167	0.167	0.00006	0.33	3756.1
(b)	0.122	0.118	0.10	0.32	1332.4
(c)	0.125	0.125	0.05	0.40	1576.3
(d)	0.084	0.076	0.15	0.38	369.1

From Figure 10 and Table II the maximum KE_f occurs when the delivery component length is minimized, and all the other moving spheres radii are maximized. The optimized KE_f using different radii spheres is more than twice the result when all radii are the same. Figure 11 shows the optimized two-stage Gauss gun, with parameter values given in Table III.

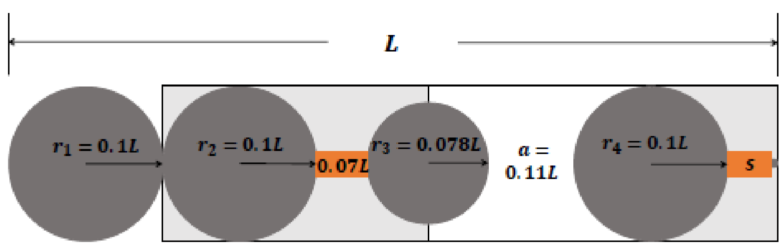

Fig. 11. Two–stage optimum MRI Gauss gun with different radii case.

Table III: Optimum Values For r_1, r_2, r_3, r_4, s, a, and KE_f/L^3

N	$\frac{r_1}{L}$	$\frac{r_2}{L}$	$\frac{r_3}{L}$	$\frac{r_4}{L}$	$\frac{r_5}{L}$	$\frac{s}{L}$	$\frac{a}{L}$	$\frac{KE_f}{L^3}$
2	0.1	0.1	0.0785	0.1	≈ 0	0.066	0.112	1019.2

For two-stage Gauss guns, not constraining the radii gives $KE_f = 1019.2\ J/m^3$, about three times the KE_f with equal radii.

C. Study Cases

In this subsection, the method used in Section IV-B is applied in real situations, where the MRI Gauss gun will be used to deliver the drug or remove clot from the body for different areas.

1) Designing MRI Gauss gun for brachytherapy delivery in the bladder: Given a tumor location on the wall of the bladder, this case study seeks to maximize the kinetic energy supplied by a Gauss gun to propel brachytherapy seeds into the tumor. The bladder is a hollow, muscular, elastic organ that sits on the pelvic floor. The urethra provides a natural opening for inserting MRI Gauss gun components into the bladder. In this case, the urethra radius and the bladder width are the constraints. A urethra male average radius of $4.25\ mm$ [19] was used as the radius constraint and a bladder transverse width of $9.6\ cm$ [20] as the total length constraint. The final constraint is the brachytherapy seed radius of $0.4\ mm$. This seed is the delivery component in the MRI Gauss gun. Using the optimization from Section IV-B, $a = 12.4\ mm$, $s = 6.6\ mm$ and $N = 3$ providing a KE_f of $147.9\ mJ$. Figure 12 (a) shows a schematic of an MRI Gauss gun inside the bladder.

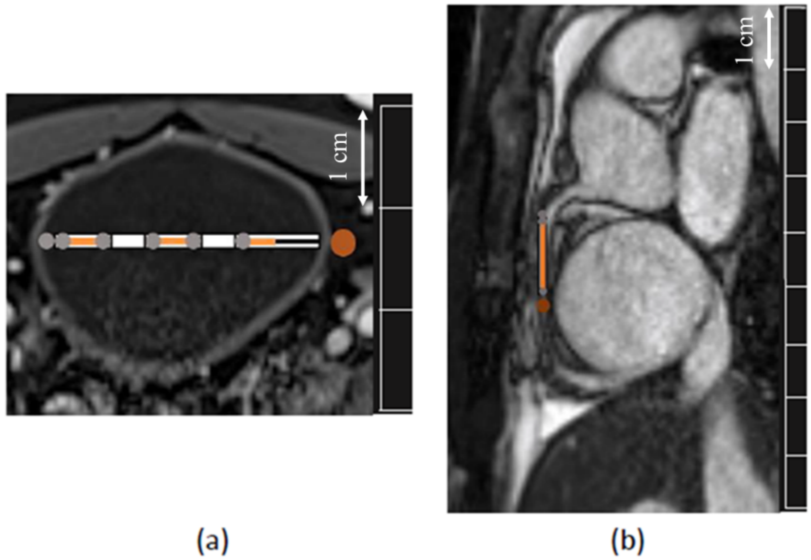

Fig. 12. Schematic showing the maximum size MRI Gauss gun inside (a) bladder and (b) coronary artery. MRI images are enlargements of Fig. 2. Targets are illustrated by brown disks.

2) Designing MRI Gauss gun for cyst fenestration in brain ventricle, entry through the spinal canal: This study case optimizes an MRI Gauss gun to deliver a drug to the brain ventricle by entering through the spinal canal. A millirobot designed to fit through a 2.5 mm channel could navigate the side or posterior subarachnoid spaces in about 50% of the population, while a device designed to fit through 1.5 mm channel would fit in more than 85% of the population [21]. This study assumes a radial constraint of 0.75 mm, to fit the 85% criterion. The delivery projectile is a brachytherapy seed with a radius of 0.4 mm. [22] reported that the length for the lateral ventricle's size depends on the age and gender as listed in Table IV.

Table IV: Measurements of Frontal Horn of Lateral Ventricle [22] and Max KE_f.

Age	Sex	Length mm	a mm	s mm	KE_f (mJ)
15–30	M	28.1 ± 2.1	2.16	1.27	1.05
31–50	M	31.7 ± 2.3	2.70	1.77	1.18
51–70	M	32.5 ± 2.3	2.82	1.89	1.20
15–30	F	27.6 ± 1.7	2.10	1.20	1.03
31–50	F	28.0 ± 1.7	2.15	1.26	1.05
51–70	F	30.1 ± 2.0	2.46	1.54	1.13

3) Designing MRI Gauss gun for firing inside the coronary artery: This case study designs an MRI Gauss gun to fire on a clot in the coronary artery. A typical entry for endoscopic access to the coronary artery is through an artery in the groin. In a similar manner, this case study proposes inserting Gauss gun components through an artery in the groin and then navigating them through the aorta to the left coronary artery. The aorta and the arteries from the groin area have larger diameters than the coronary artery. The coronary artery has an average diameter of 4.6 mm and a 19 mm length [23]. Therefore, the radius was constrained to be no larger than 2.3 mm and the completed Gauss gun constrained to be no longer than $L = 19\ mm$. The optimal parameters are $s = 21\ mm$, $a = 0$, $N = 1$ and $KE_f\ =\ 10\ mJ$. Figure 13 (b) shows a schematic of an MRI Gauss gun inside the coronary artery.

V. Gauss Gun Hardware Experiments

One-stage and two-stage Gauss guns were implemented in hardware experiments as shown in Figure 13.

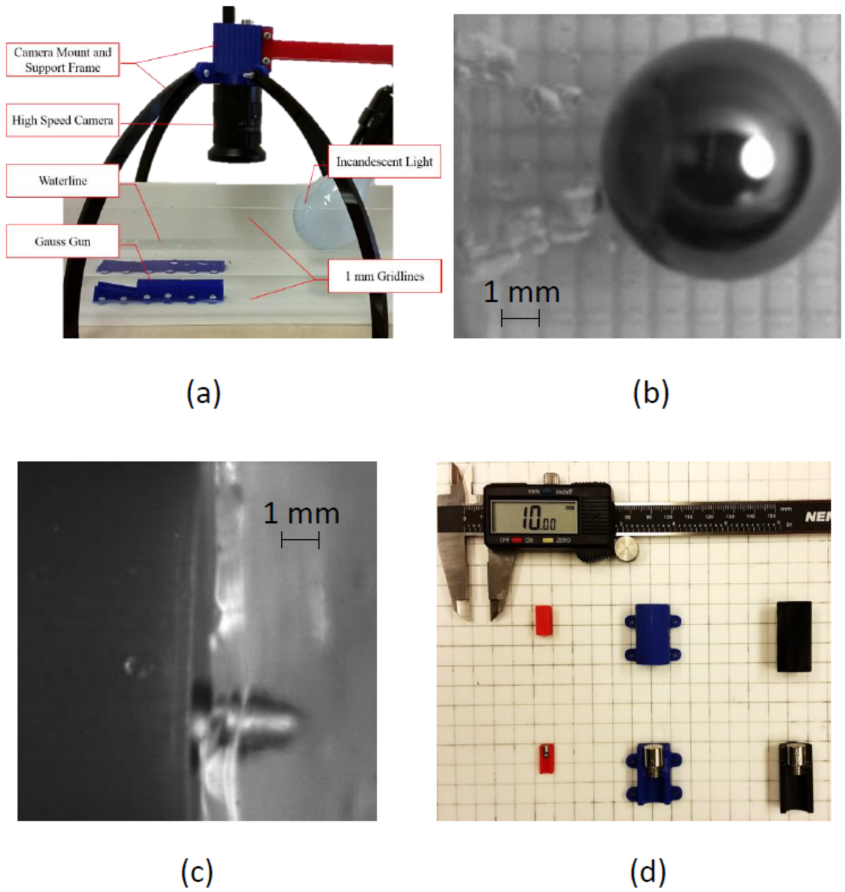

Fig. 13. Lab implemented (a) one-stage, (b) after firing underwater Gauss gun projectile, (c) firing screw into gelatin and (d) cross sections.

The MRI Gauss gun use steel spheres (E52100 Alloy, McMaster 992K41) for the magnets and titanium for spacers, which provides several benefits: (1) inside an MRI, steel is a stronger magnet than neodymium. (2) Spacer length is arbitrary and can be chosen to maximize energy. (3) Leaving multiple magnets in tissue is potentially dangerous, leading, e.g., to bowel necrosis, perforation, volvulus, sepsis and possible death [24] [25]. In contrast, the steel bearing spheres used in this paper lose their magnetism when removed from the magnetic field. (4) MRI enables imaging and control to assemble components at the target. (5) MRI enables controlled removal of components.

For Gauss guns tested outside an MRI, the first sphere of each stage was replaced by a neodymium magnet as a magnetic source to magnetize other spheres. The Gauss gun has been attached to a test bed with a Basler acA2040-90μm camera to record the firing velocity to compute KE_f.

A. One and Two-stage Gauss Guns Firing in Air

This section presents the experiment results for one-stage Gauss gun and two-stage Gauss gun using the same sphere radii for both cases with different spacers.

1) One-Stage Gauss gun: Figure 14 shows measurements of the projectile kinetic energy for different $r = L$ and Table V shows the s and L values used to find KE_f measurements.

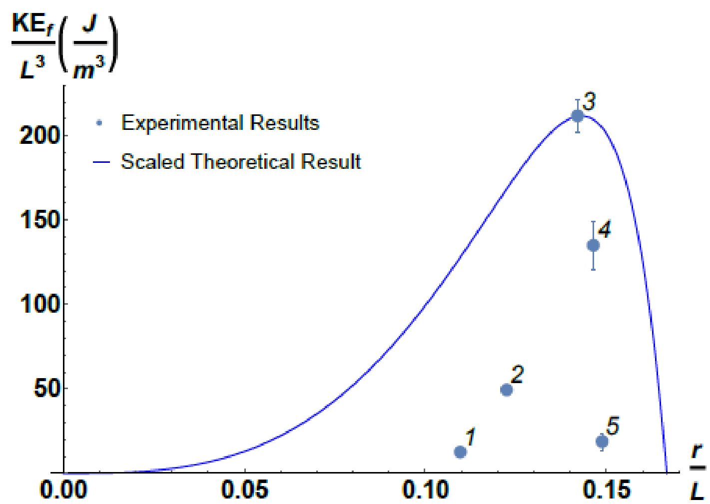

Fig. 14. One-stage experiment results when $r = 4.76$ compared to scaled theoretical result, the average values for s, L, V_0 and KE_f are in Table V.

Table V: One-Stage Gauss Gun Experiment Results Firing in Air Using Steel Sphere With $r = 4.76$ mm. Each Test Included 5 Trials.

Trial	s (mm)	L (mm)	v_0 (mm/s)	KE_f (mJ)
1	14.86	43.43	0748 ± 36.0	1.01 ± 0.10
2	10.28	38.86	1268 ± 31.2	2.91 ± 0.14
3*	4.95	33.53	2100 ± 48.1	7.98 ± 0.37
4	3.93	32.51	1600 ± 83.9	4.64 ± 0.49
5	3.43	32.00	0576 ± 82.4	0.17 ± 0.17

* signifies the optimum

Each one-stage Gauss gun was fired 5 times, and the average firing velocity was used to find KE_f, using the following equation:

$$KE_f = \frac{1}{2} m \cdot v_0^2. \tag{22}$$

Where m is the sphere's mass which is 3.63 g for all spheres, and v_0 is the projectile velocity. Figure 14 shows that the optimum KE_f occurs when $r = L = 0.142$. Results in Figure 14 have values less than the theoretical results due to friction, sound and heat energy loss. Additionally, the actual size of the spheres can vary from the theoretical size and in the theoretical calculation all the spheres are magnets whereas the experiment has only one magnetic component. On the other hand, the point where the maximum kinetic energy occurs matches the calculation in Figure 9, as does the general shape of the curve.

2) Two–Stage Gauss gun: Figure 15 shows measurements of the projectile kinetic energy for different r/L and Table VI shows the s and L values used to find KE_f measurements.

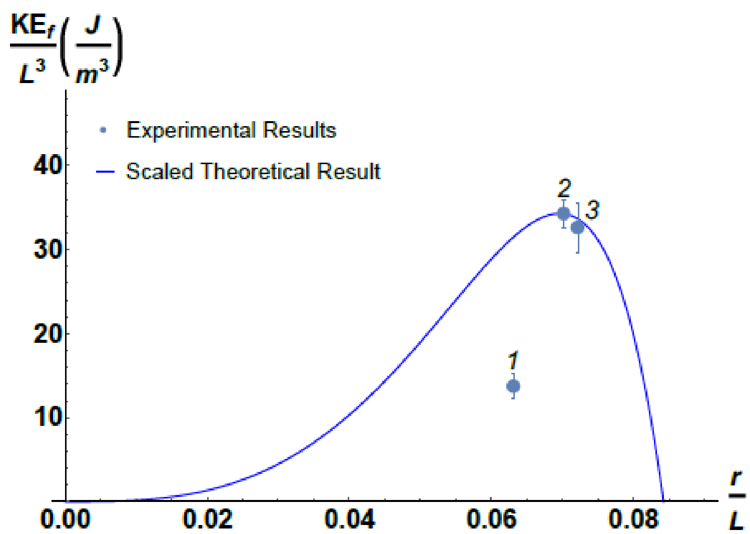

Fig. 15. Two-stage experiment results when $r = 4.76$ compared to scaled theoretical result the average values for s, L, v0, a and KE_f are in Table VI.

Table VI: Two-Stage Gauss Gun Experiment Results Firing in Air Using Steel Sphere with r = 4.76 mm. Each Test Included 5 Trials.

Trial	s (mm)	a (mm)	L (mm)	v_0 (mm/s)	KE_f (mJ)
1	9.2	10	75.5	1808 ± 95.92	5.90 ± 0.02
2*	5.3	10	67.8	2432 ± 59.13	10.7 ± 0.52
3	3.2	13.4	65.9	2272 ± 107.1	9.35 ± 0.86

* signifies the optimum

Each two-stage Gauss gun was fired 5 times, and the average firing velocity was used to find KE_f, using (22). Figure 15 shows that the optimum KE_f occurs when $r/L =$ 0.07. As with the single–stage Gauss gun, results in Figure 15 have values less than the theoretical results due to mechanical losses, but the curve and point of maximum kinetic energy match the calculation in Figure 8.

B. Firing Gauss Gun Immersed in Liquid

The MRI Gauss guns in [15] were unable to fire in liquid due to high viscous damping on the ball bearings used inside the trigger and intermediate stages. Instead, tests were performed in air by placing the gauss gun on floats. To overcome this issue, alternative designs for the trigger and intermediate stages were fabricated with thin discs of sheet metal capping the ends. When the Gauss gun fires, the impact force is transmitted through the foil to the next component. This design allows the ball bearings to travel through a pocket of air of length a and lessens the energy loss between stages. The projectile is designed to be launched from the Gauss gun and cannot avoid the viscous damping, but it can be minimized by pushing the entire mechanism against the target and streamlining the projectile.

To evaluate the effect of various capping materials on the performance of a Gauss Gun, sheets of 0.1 mm thick aluminum, brass and titanium were tested in an underwater setup shown in Figure 14(a). The underwater experimental setup has 1 mm grid lines etched into its base and an overhead high-speed camera, which allows us to measure distance traveled per frame (at 400 fps) and determine the projectile's exit velocity. In this experiment, we rigidly attached a firing stage and a capped intermediate stage to the base of the setup, with the end of the firing stage directly under the camera. A single ball bearing was used as a trigger and was released from the end of a small guide ramp to ensure a direct impact on the intermediate stage. For each of these materials, a thinner cap variant was also tested to evaluate whether capping inherently improves exit velocity. An additional experiment was conducted to determine the effect of cap thickness on exit velocity, using stainless steel discs of 0.025, 0.051, 0.076, and 0.127 millimeters thick, as cap materials. Each cap variation was tested ten times (after allowing initial deformation to occur), the results of these experiments are displayed in Figures 16 and 17 below.

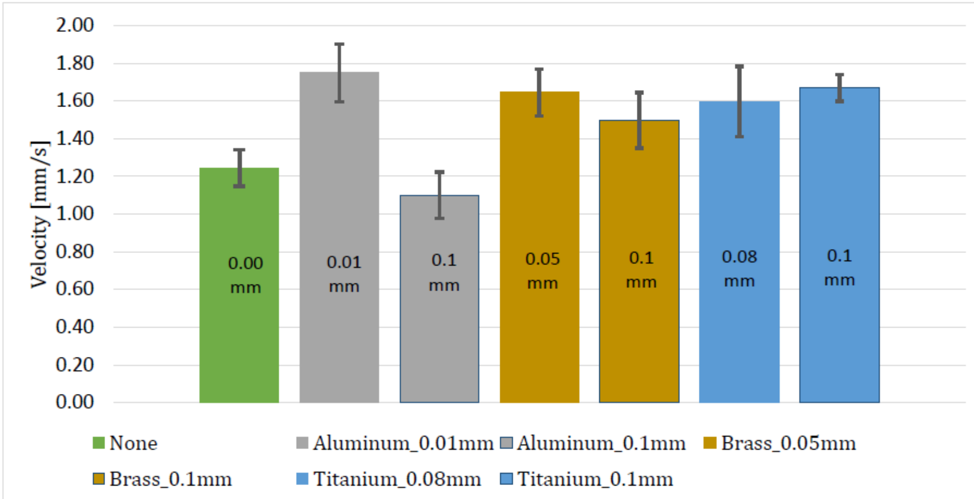

Fig. 16. Underwater capping materials experiment results representing average values of ten trials.

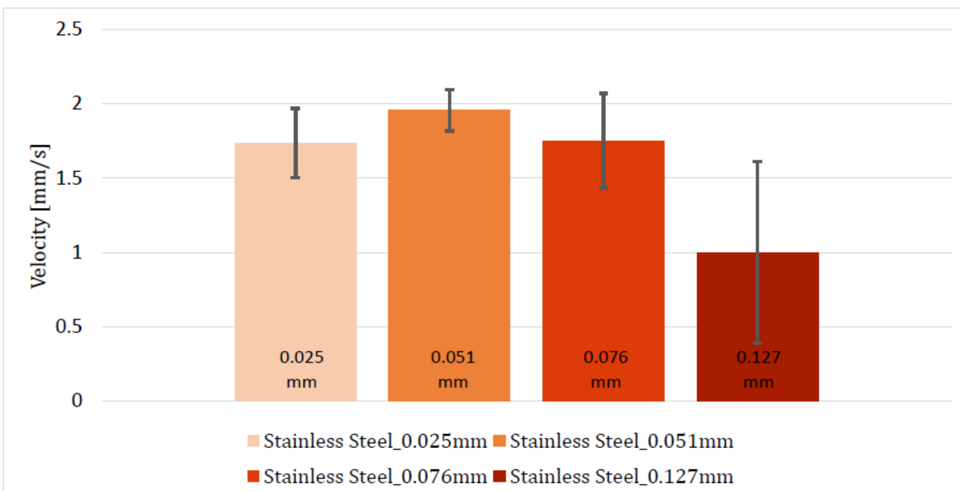

Fig. 17. Underwater cap thickness experiment results representing average values of ten trials.

All cap variations, excluding the 0.1-millimeter-thick aluminum, showed higher exit velocities than the control experiment performed with no cap. As can be seen in Figures 16 and 17, many of the tested cap materials had quite large standard deviations. For the cap variations shown in Figure 16, the thinner caps all have greater standard deviations than their 0.1 mm counterparts, except for brass. In Figure 17, the standard deviations are even greater for the thicker stainless-steel variations. While at first glance this seems counterintuitive, the stainless steel was unfortunately mildly magnetic and most likely altered the magnetic field of the Gauss gun enough to cause inconsistent impacts on the firing stage. This would explain the large inconsistency in the 0.127 mm stainless steel cap. Certain cap materials had large numbers of *misfires*, in which so much energy is lost to damping that the projectile fails to overcome the magnetic force of the firing stage and does not exit the gauss gun. Misfires mostly occurred in softer metals like aluminum and brass, which show visible deformation in the form of a dimple after the first few uses. The formation of a dimple heavily reduces the energy being transferred to the projectile and creates large inconsistencies during the first few firing attempts, but once this initial deformation occurs the firing results become more consistent. Due to this, materials that showed high initial deformation were fired several times prior to testing, to allow a dimple to form. While this gave more consistent results than the initial firings, a dimple occasionally causes impacts to not transfer cleanly to the firing stage, usually resulting in larger numbers of misfires. A few other cap variations suffered from frequent misfiring, such as the 0.127 mm stainless steel, the 0.1 mm aluminum and the control with no cap. For the control experiment without a cap, misfires occurred more often than successful fires, which is expected due to the large amount of viscous damping. Misfires of the 0.127 mm stainless steel caps most likely occurred due to mild magnetization creating inconsistent levels of damping, while the 0.1 mm aluminum always caused too much damping in the system. Along with high numbers of misfires, these two caps also had the lowest average exit velocities, even lower than that of the control. Another important consideration to note is that while the 0.01 mm aluminum achieved the greatest exit velocity, this cap was particularly prone to tearing and consistently failed after 3 cycles while every other cap material was able to operate for over 50 cycles without material failure. There is no general trend shown for thinner materials having the highest exit velocity, nor is a certain material obviously superior to all others. From the data gathered, the best observations we can make are that:

- Each material will have an ideal thickness for this application such that the cap will take several cycles to fail but be thin enough to absorb as little force as possible.
- Materials with a higher coefficient of restitution are ideal as they more readily transfer force, rather than absorbing the impact.
- Biocompatible materials should be used for all external components.
- The material should be non-ferrous as the MRI will otherwise magnetize the cap and alter the Gauss gun's inherent magnetic field, potentially leading to increased misfire and decreased exit velocities

Based on these considerations, titanium is the most compatible material to use for capping the trigger stage and intermediate stages due to its high coefficient of restitution, non-magnetic nature and good biocompatibility.

C. Underwater Firing Demonstration in Clinical MRI

The MRI Gauss gun was tested in a Siemen's 1.5T MRI scanner. Because the MRI magnetizes all steel spheres, the magnets used for benchtop tests were replaced by steel spheres. A 5 cm wide agarose gel target was placed inside a 5 cm diameter tube sealed at one end, the tube was then filled with water and placed in the MRI and imaged, as shown in Figure 18 (a).

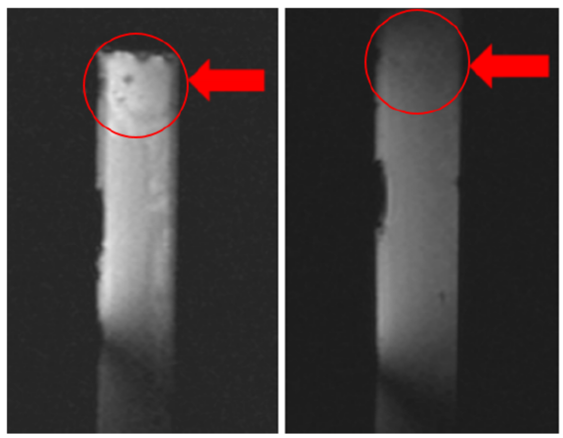

(a) (b)

Fig. 18. MRI image of phantom and agarose gel target before and after firing the Gauss gun.

Next a one-stage Gauss gun was placed at the entrance of the tube and steered to the agarose target by moving the motorized patient bed out, so the MRI's fringe field pulled the Gauss gun to the target. To trigger the Gauss gun, a steel sphere was inserted into the tube. The sphere initially moved due to gravity, then was accelerated by magnetic attraction to the first stage of the gauss gun and triggered the Gauss gun. After firing, the Gauss gun was removed from the tube and a second MRI scan was performed. Figure 18 shows the gel before and after firing. It can be noticed that the gel is cleared away from the center of the tube after firing. Additional experiments were performed using various projectiles to penetrate a banana and a cow heart within the MRI. A cow heart penetrated using a needle projectile approximately 12 mm long is shown in Figure 19, the green markings on the projectile indicate a distance of 1 mm. The projectile was fired in air using a single stage gauss gun with a component radius of 4.75 mm.

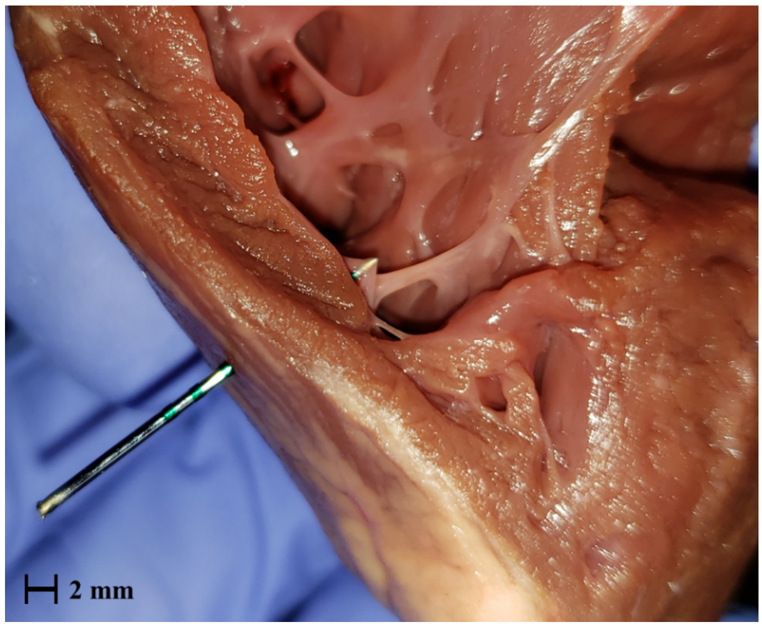

Fig. 19. Cow heart wall penetrated by MRI Gauss Gun projectile.

The projectile shown in Figure 19 penetrated through the outer wall of the cow heart to a total depth of 10 mm, proving that the MRI can provide enough forced to penetrate cardiac muscle with devices on a centimeter scale. While downsizing the device to milli and micro scales will see significantly reduced forces, it is possible a stronger MRI could provide enough force for these devices to operate.

VI. Gauss Gun Conclusion

This paper presented a model, optimization, applications and experiments for MRI Gauss guns in air and underwater. The experimental results for one-stage and two-stage Gauss gun agree with the analysis and calculations. An analysis was performed to optimize the MRI Gauss gun with a length constraint. The MRI Gauss gun depends on the magnetic field generated by the MRI itself, and it can be self-assembled into a larger tool to increase the final kinetic energy for the delivery component. The bladder, brain ventricle, and coronary artery were used as case studies. Gauss gun experiments inside and outside the MRI demonstrated performance in air and underwater that align with theoretical results. Reduced scaling of the Gauss guns is limited by manufacturability of the housings and will require stronger MRI fields to achieve similar results. Future work should focus on material selection for bio-compatibility and neutral buoyancy, customized design of the delivery component, motion planning of components, and automatic disassembly of the Gauss gun, in preparation for in vivo tests.

VII. Drift Node Introduction

Sections VII-XI present the work of multiple labs on designing degradable drift nodes. My contributions to this project include the design and fabrication of shell components, sensor testing and evaluation, waterproofing, and conducting experiments.

Oceanic and offshore surveying has many industrial applications but is notably important in environmental monitoring as rising sea levels, regular sediment erosion and powerful storm systems alter our coasts and impact thousands of people each year. The goal of the drift node project is to develop a cheap, easily manufactured, fully degradable and environmentally benign sensor package for monitoring hazardous or inaccessible aquatic environments. Hundreds of these small devices could be released near a target location, drift through it collecting data, wirelessly transmit the data via satellite systems, and safely dissolve when the task is complete. Sensors can be easily traded in and out on the drift nodes to meet desired capabilities. Examples of these sensors include; sonar devices for depth sensing, pressure sensors, salinity gauges, inertial measurement unit (IMU) to track acceleration in three dimensions, GPS for location data, temperature probes, etc. A previous design for node drifters was created by Rekleitis et al. for the tracking of ocean currents and shallow coral reefs [26, 27]. This design utilized a 2-foot-long PVC tube shell to maintain neutral buoyancy, with the electronics rigidly attached to an interior acrylic plate which slides out of the shell. The estimated cost of this original design was $250, with the most expensive components being the Raspberry Pi. The design presented in this report is of significantly reduced size and has been optimized for ease of manufacturing and assembly while collecting consistent data.

Section VIII. Circuitry and Shell Design

The drift node was initially altered from the design presented by Rekleitis et al. to reduce size and weight but utilized similar sensors. One of the main design goals was to make the manufacturing process simple, which was achieved using a 3D printer. The second version of the drift node featured a fully 3D printed shell of PLA that was sealed using O-rings, an Adafruit 9 degrees of freedom IMU breakout board, an Adafruit GPS breakout board, an Adafruit ADS1115 16-Bit ADC, a JSN-SR04T-2.0 ultrasound range finder, a Raspberry Pi camera module, a Raspberry Pi Zero-W, a Pimoroni LiPo SHIM and two 3.7v 500mAh Adafruit 1578 Lithium Ion Polymer Batteries. The version 2 design is shown in Figure 20 and the wiring diagram for it is shown in Figure 21.

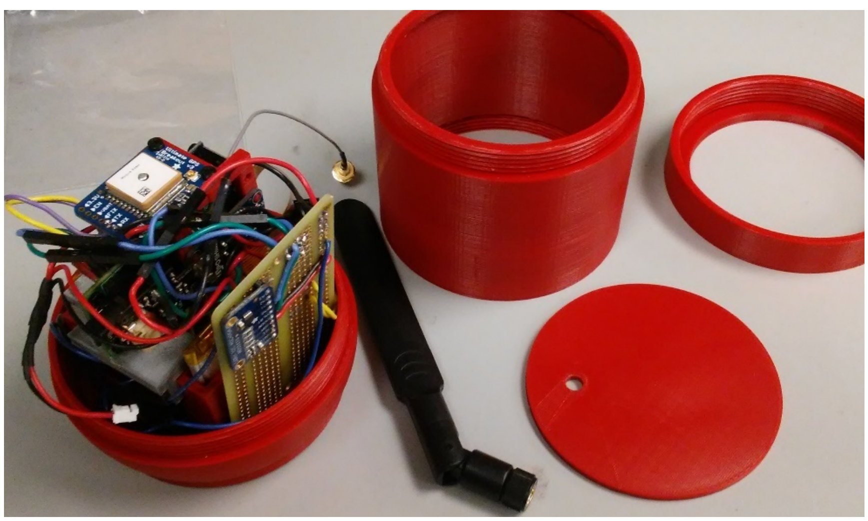

Fig. 20. Drift Node Version 2 shell and electronics.

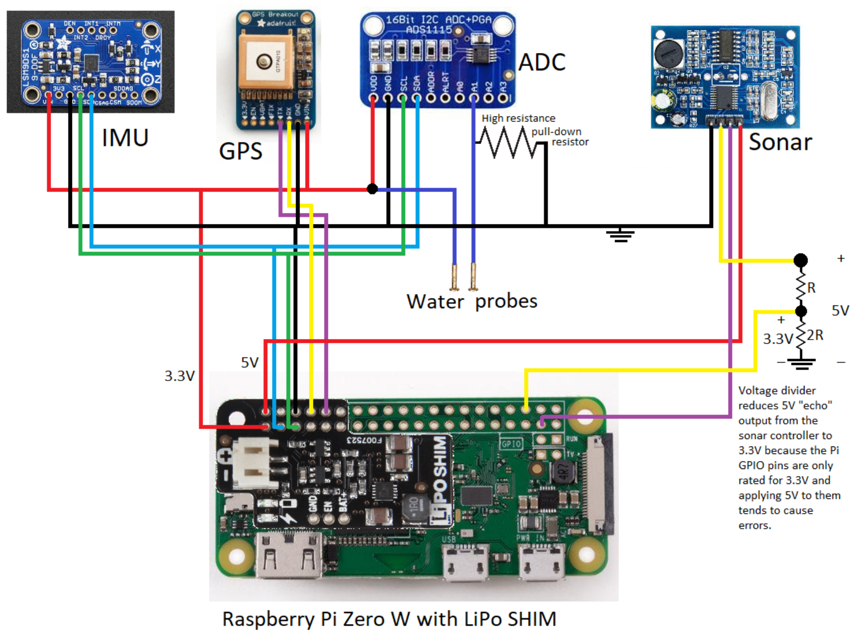

Fig. 21. Wiring diagram for Drift Node Version 2.

This design had several issues that were addressed in the next iteration. Among these issues were balance problems that caused it to be easily knocked around by waves, relatively short battery life, a cramped electronics package and most importantly the ultrasound range finders performed very poorly in water and had to be replaced. For version 3 the CPU was upgraded to a Raspberry Pi 3, the range finder was replaced with a Blue Robotics Ping Sonar, the batteries were replaced with 3.7V 6600mAh Adafruit Lithium Ion Battery Packs and the shell was redesigned to properly house the new electronics. Following these modifications, the estimated price of a drift node increased to around $500, mostly due to the $300 ping sonar. Additional adjustments were made to the shell to increase ease of access to internal components and improve balance such that the node now rides waves and if flipped, will immediately right itself. A ballast weight was placed in the bottom of the shell to help balance the node. An exploded view of drift node version 3 is shown in Figure 22, with the electronics package representing the Raspberry Pi 3, IMU, GPS board, ADC, and a custom PCB board to fit the components.

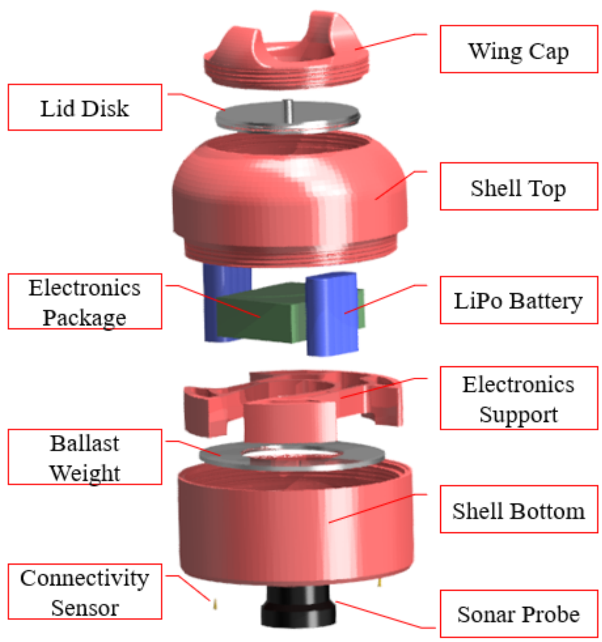

Fig. 22. Exploded view of Drift Node Version 3

Buoyancy and center of mass calculations were performed on the design of version 3 to ensure the node can maintain itself in an upright position for optimal data collection. Center of mass is calculated using

$$\frac{\sum_i M_i \cdot x_i}{M_T}. \tag{23}$$

Where M_i is the mass of each component, x_i is a component's relative position from the bottom of the node and M_T is the total mass of the node. Using equation 23, the center of mass of the drift node is located 49.1 mm above the base of the node, while the entire height of the node is approximately 140 mm. When considering only internal components, their center of mass is 20.3 mm above the base of the node. Most of the drift node's weight is well below its midpoint, meaning that while the waterline sits above the center of mass of the node, tilting motion due to waves will be counteracted by torque generated from the internal weight. If the buoyant force of the drift node is not too great, tipping over is not an issue. Should the drift node be completely flipped by a wave, it will still restore itself to an upright position if it cannot find another point of balance. The top half of the drift node is rounded to prevent the existence of another stable balance point.

Buoyancy can be determined by comparing the total weight of the node to the buoyant force acting upon the node by displaced water. Buoyant force, F_B, can be calculated by

$$F_B = V_d \cdot \rho_{H_2O} \cdot g. \tag{24}$$

Where V_d is the volume of water displaced, ρ_{H_2O} is the density of the water, and g is the acceleration due to gravity. Should the drift node be completely submerged it would generate a buoyant force of approximately 19.5 N, which is much greater than its force of weight at 9.46 N. If only the lower half of the drift node was submerged, the buoyant force acting upon it would be approximately 11.35 N. If the node was only submerged up to its center of mass, the buoyant force would be 7.95 N, meaning the drift node will rest in the water somewhere above the center of mass and below the midpoint of the node. The exact height the node rests at in water is dependent upon the salinity of the water but should remain well above the center of mass. From the calculations performed using equations 23 and 24, it was determined that the version 3 drift node should maintain a generally upright position throughout testing and will right itself if flipped over.

Drift node code was written using Python and run through the Raspberry Pi via SD card. The nodes were coded to start each component as soon as the Pi is powered on, data is collected simultaneously from each sensor, accompanied with a timestamp and saved to the SD card in a single file. This file can then be processed using a separate program to plot the path travelled and correlate the appropriate sonar, IMU and ADC data. Further processing can be done using the IMU and sonar data to determine wave height and with a full fleet of sensors a subsea map could be formed.

Section IX. Dissolvable Polymers and Circuits

While the shell of the current design is made of PLA, Dr. Megan Robertson's lab in the Chemical Engineering Department at University of Houston is working to replace this material with a sturdy but dissolvable material that can also be 3D printed. Her lab has succeeded in creating several different polymer materials that can dissolve in a weak acid mixture in just a matter of hours, but do not yet possess the mechanical properties needed. This project is still ongoing, but as of now they have created several polymers with better mechanical and thermal properties that may be 3D printable while still showing similar degradation properties to the previous samples. The degradation of some water-degradable thermosets developed by Dr. Robertson's lab are shown in Figure 23.

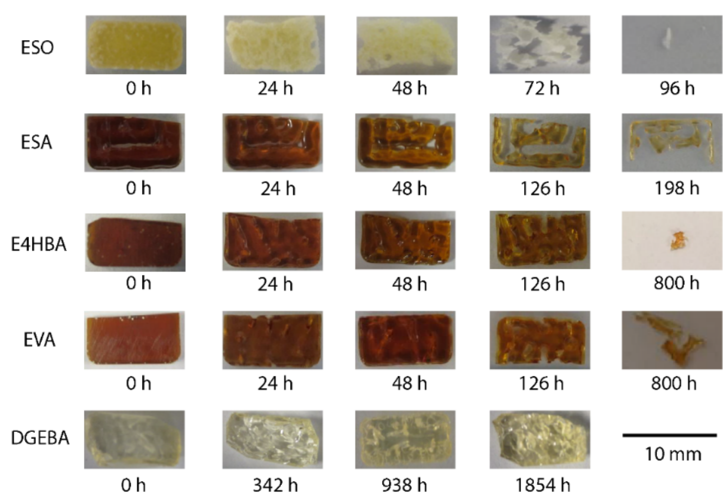

Fig. 23. Water-degradable thermosets left in a Basic solution (3 wt% NaOH) at 80 °C.

Cunjiang Yu's lab in the Mechanical Engineering Department at University of Houston is developing dissolvable circuitry that may eventually be able to replace some components of our electronics package, but it is in very early stages. Thus far they have been able to create small RLC circuits that fully dissolve in saltwater within 24 hours. While the circuits are currently too small and weak to provide any meaningful function to a device, their process shows great promise and perfectly achieves the desired goal of the drift node project. Figure 24 shows an example of these RLC circuits degrading in a petri dish filled with seawater collected from the Gulf of Mexico in Gulfport, Mississippi.

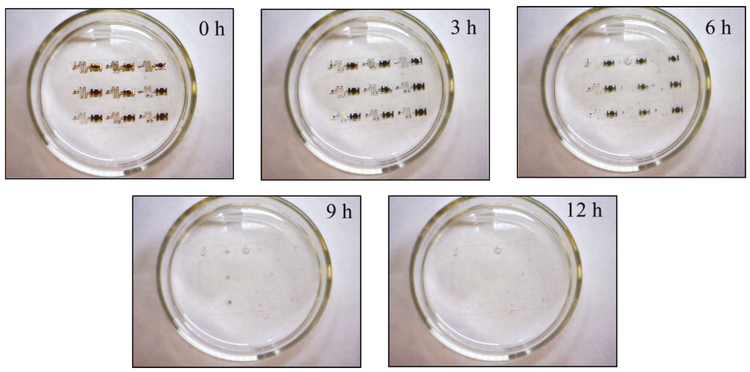

Fig. 24. RLC circuits degrading over time in seawater from Gulfport, Ms.

Section X. Drift Node Tests

Several tests were performed in both freshwater and saltwater, with the longest test occurring in Gulfport, Mississippi over a span of 5 hours. Prior tests were preliminary and focused on verifying the functionality of electronic components and the reliability of the shell. Preliminary testing led to the replacement of the original sonar with the ping sonar, and upgrades made to the batteries and Raspberry Pi. The first deployment of the version 2 node was done in Clear Lake, Texas and was used to verify the functionality of the GPS data and sonar data from the ultrasound range finder. During this test, three nodes drifted away from shore for roughly 30 minutes before being recovered. Figure 25 shows the plotted GPS data from the Clear Lake test overlaid onto a satellite image of the area from Google Maps.

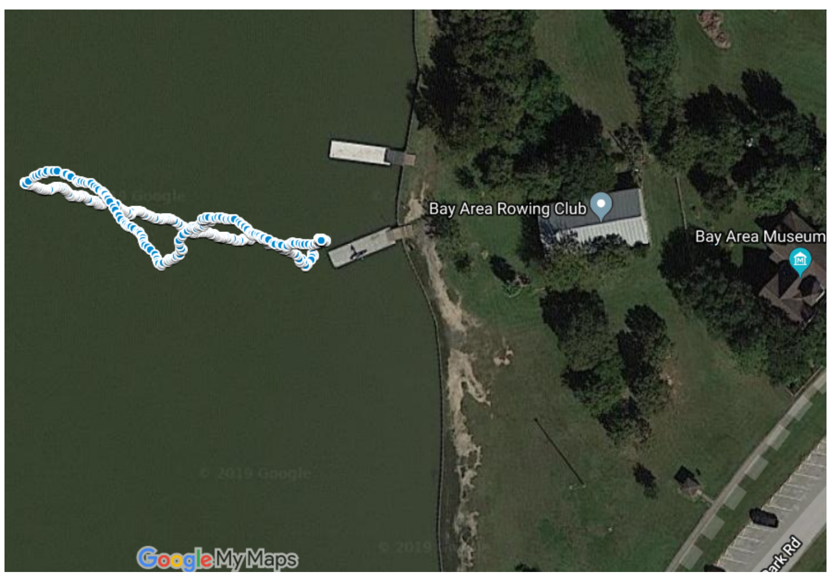

Fig. 25. GPS path data gathered by a version 2 drift node in Clear Lake, Tx.

Upon examining the data, the GPS path accurately followed the path traveled by the nodes, but the sonar data was sporadic and inconsistent. Further tests were performed with just the sonar data and it was determined that the ultrasound range finder needed to be replaced with the more reliable and more accurate Blue Robotics ping sonar. The battery life of the version 2 drift node was found to be at most 8 hours, but this dropped to 4.5 hours after the addition of the ping sonar. The required milliamp hours needed to operate the full drift node for our goal of 12 hours was then calculated and the appropriate batteries purchased. Additional battery life tests were performed on the version 3 nodes, which consistently met or exceeded the 12-hour mark.

After redesigning the drift nodes to accommodate the ping sonar, Raspberry Pi 3 and larger batteries, waterproofing and self-righting experiments were conducted. The version 3 drift nodes were able to maintain a dry interior for over 12 hours in shallow water using greased O-rings along the seals. The shape and design of version 3 allowed the nodes to immediately self-right when flipped over or turned on their sides. Another full test was conducted in Texas City, Texas with the version 3 nodes to verify their complete functionality. During this test, two drift nodes were allowed to drift for around 3 hours. Unfortunately, possibly due to weather conditions, the GPS signal did not function during this test. Sonar data seemed to match the know depths of the area, both the IMU data and ADC data were consistent, and waterproofing kept the internal components dry. Figure 26 shows two version 3 drift nodes floating in the Gulf of Mexico in Galveston, Texas, following the Texas City launch.

Fig. 26. Version 3 drift nodes in the surf of Galveston, Tx.

A single drift node was launched for roughly 2 hours in Lake Conroe, Texas to verify the GPS functionality within the version 3 nodes. During this test, all components of the drift node functioned properly for its entirety. Following this test, wireless transmission of data became the focal point along with fixes to small bugs in the code in preparation for the Gulfport experiment.

During the Gulfport test three drift nodes were tied together and drifted freely through the Gulf of Mexico while operating continuously for 5 hours. A Verizon Jetpack wireless hotspot was placed inside each drift node to upload the drift node data to a website as it was collected. The nodes drifted approximately 1.57 miles and were relocated using the latest GPS coordinates uploaded to the website and a separate GPS tracking device as a backup. Figure 27 shows a plot of the GPS coordinates collected from one drift node overlaid onto a map of the area from Google Maps, along with the corresponding depth sensor readings.

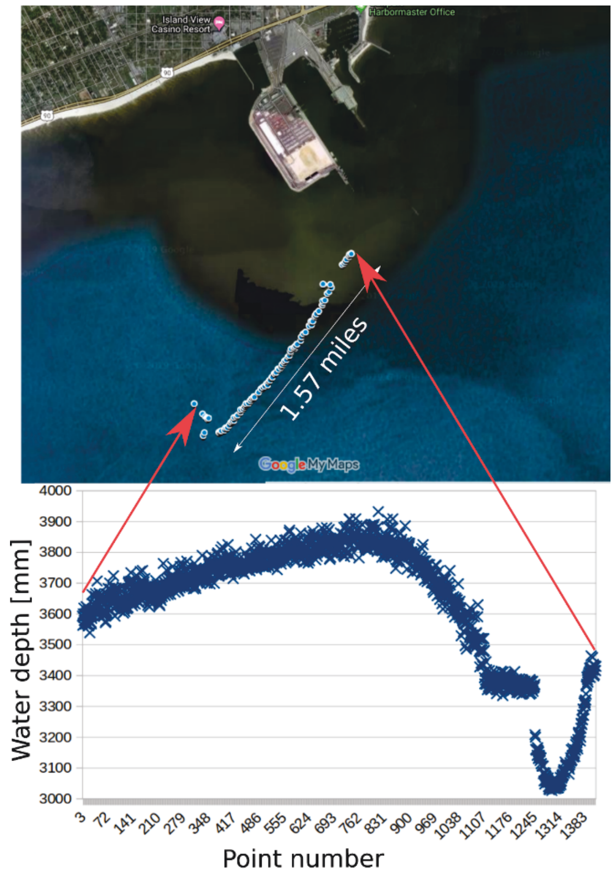

Fig. 27. Map of GPS coordinates and corresponding depth data for Gulfport experiment.

During the Gulfport testing, GPS signal was spotty at some points and can be seen as gaps in the collected data in Figure 23. Further testing of the GPS boards found them to be unreliable and they will be replaced for future experiments. The depth data collected during this experiment correlates well with the known depth of the area. Overall the test was successful, showing that the current drift node design is capable of gathering consistent GPS, depth and IMU data for several hours while wirelessly transmitting the data to our server as it was collected.

Section XI. Drift Node Conclusion

Offshore environmental surveying is an increasingly important field of science as mankind evaluates the impacts of global warming, rising sea levels and large storm systems. Low cost, mass produced, biodegradable sensor packages could provide an optimal solution for surveying large areas in harsh climates and inaccessible waters. Drift nodes meet most of these criteria already, and advancements are being actively made to develop electronic devices that dissolve in saltwater and environmentally benign, degradable polymers that can be 3D printed. The current drift node design shows that relatively cheap sensors could be mass produced via 3D printing and be used to gather important environmental data without needing to be recovered.

References

[1] C. T. Dotter and M. P. Judkins, "Transluminal treatment of arteriosclerotic obstruction: description of a new technic and a preliminary report of its application," Circulation, vol. 30, no. 5, pp. 654–670, 1964.

[2] E. J. Benjamin, M. J. Blaha, S. E. Chiuve, M. Cushman, S. R. Das, R. Deo, S. D. de Ferranti, J. Floyd, M. Fornage, C. Gillespie, C. R. Isasi, M. C. Jimenez, L. C. Jordan, S. E. Judd, D. Lackland, J. H. Lichtman, L. Lisabeth, S. Liu, C. T. Longenecker, R. H. Mackey, K. Matsushita, D. Mozaffarian, M. E. Mussolino, K. Nasir, R. W. Neumar, L. Palaniappan, D. K. Pandey, R. R. Thiagarajan, M. J. Reeves, M. Ritchey, C. J. Rodriguez, G. A. Roth, W. D. Rosamond, C. Sasson, A. Towfighi, C. W. Tsao, M. B. Turner, S. S. Virani, J. H. Voeks, J. Z. Willey, J. T. Wilkins, J. H. Wu, H. M. Alger, S. S. Wong, and P. Muntner, "Heart disease and stroke statistics—2017 update: A report from the american heart association," Circulation, 2017. [Online]. Available: http://circ.ahajournals.org/content/early/2017/01/25/CIR.0000000000000485

[3] R. C. Ritter, M. S. Grady, M. A. H. III, and G. T. Gillies, Computerintegrated Surgery: Technology and Clinical Applications. The MIT Press, 1996, ch. 26 Magnetic Stereotaxis: Computer-Assited, Image- Guided Remote Movement of Implants in the Brain, pp. 363–370.

[4] K. Ishiyama, M. Sendoh, A. Yamazaki, and K. Arai, "Swimming micro-machine driven by magnetic torque," Sensors and Actuators A: Physical, vol. 91, no. 1, pp. 141–144, 2001.

[5] A. Chanu, O. Felfoul, G. Beaudoin, and S. Martel, “Adapting the clinical MRI software environment for real-time navigation of an endovascular untethered ferromagnetic bead for future endovascular interventions,” Magn Reson Med, vol. 59, no. 6, pp. 1287–1297, Jun. 2008.

[6] P. Vartholomeos, M. Akhavan-Sharif, and P. E. Dupont, “Motion planning for multiple millimeter-scale magnetic capsules in a fluid environment,” in IEEE Int. Conf. Rob. Aut., May 2012, pp. 1927– 1932.

[7] P. Vartholomeos, C. Bergeles, L. Qin, and P. E. Dupont, “An MRIpowered and controlled actuator technology for tetherless robotic interventions,” Int. J. Rob. Res., vol. 32, no. 13, pp. 1536–1552, 2013.

[8] A. Becker, O. Felfoul, and P. E. Dupont, “Simultaneously powering and controlling many actuators with a clinical MRI scanner,” in IEEE/RJS International Conference on Intelligent Robots and Systems (IROS), 2014, pp. 2017–2023.

[9] A. Bigot, C. Tremblay, G. Soulez, and S. Martel, “Magnetic resonance navigation of a bead inside a three-bifurcation pmma phantom using an imaging gradient coil insert,” Robotics, IEEE Transactions on, vol. 30, no. 3, pp. 719–727, June 2014.

[10] W. K. Cho, J. A. Ankrum, D. Guo, S. A. Chester, S. Y. Yang, A. Kashyap, G. A. Campbell, R. J. Wood, R. K. Rijal, R. Karnik, R. Langer, and J. M. Karp, “Microstructured barbs on the north american porcupine quill enable easy tissue penetration and difficult removal,” Proceedings of the National Academy of Sciences, vol. 109, no. 52, pp. 21 289–21 294, 2012. [Online]. Available: http://www.pnas.org/content/109/52/21289.abstract

[11] O. Felfoul, A. Becker, C. Bergeles, and P. E. Dupont, “Achieving commutation control of an MRI-powered robot actuator,” IEEE Trans. on Robotics, vol. under review, 2014.

[12] M. Mahvash and P. Dupont, “Mechanics of dynamic needle insertion into a biological material,” Biomedical Engineering, IEEE Transactions on, vol. 57, no. 4, pp. 934–943, April 2010.

[13] J. A. Rabchuk, “The gauss rifle and magnetic energy,” The Physics Teacher, vol. 41, no. 3, pp. 158–161, 2003.

[14] D. Kagan, “Energy and momentum in the gauss accelerator,” The Physics Teacher, vol. 42, no. 1, pp. 24–26, 2004.

[15] A. T. Becker, O. Felfoul, and P. E. Dupont, “Toward tissue penetration by mri-powered millirobots using a self-assembled gauss gun,” in Robotics and Automation (ICRA), 2015 IEEE International Conference on. IEEE, 2015, pp. 1184–1189.

[16] R. Schill, “General relation for the vector magnetic field of a circular current loop: a closer look,” Magnetics, IEEE Transactions on, vol. 39, no. 2, pp. 961–967, Mar 2003.

[17] D. Meeker, “Finite Element Method Magnetics,” www.femm.info.

[18] D.-X. Chen, J. A. Brug, and R. B. Goldfarb, “Demagnetizing factors for cylinders,” IEEE Transactions on magnetics, vol. 27, no. 4, pp. 3601–3619, 1991.

[19] J. Talati, “Urethral dilatation.” JPMA. The Journal of the Pakistan Medical Association, vol. 39, no. 3, pp. 79–83, 1989.

[20] M. A. K. Mohamad Ghosn, personal communication.

[21] B. J. Nelson, I. K. Kaliakatsos, and J. J. Abbott, “Microrobots for minimally invasive medicine,” Annual review of biomedical engineering,vol. 12, pp. 55–85, 2010.

[22] B. Parija, N. Sahu, S. Rath, and R. Padhy, “Age-related changes in ventricular system of brain in normal individuals assessed by computed tomography scans,” Siriraj Medical Journal, vol. 66, no. 6, pp. 225– 230, 2017.

[23] P. S. Douglas, J. Fiolkoski, B. Berko, and N. Reichek, “Echocardiographic visualization of coronary artery anatomy in the adult,” Journal of the American College of Cardiology, vol. 11, no. 3, pp. 565–571, 1988.

[24] C. for Disease Control and Prevention, “Gastrointestinal injuries from magnet ingestion in children–united states, 2003-2006,” MMWR: Morbidity and Mortality Weekly Report, vol. 55, no. 48, pp. 1296–1300, 2006.

[25] M. F. Kircher, S. Milla, and M. J. Callahan, “Ingestion of magnetic foreign bodies causing multiple bowel perforations,” Pediatric radiology, vol. 37, no. 9, pp. 933–936, 2007.

[26] Boydstun, D., Farich, M., Iii, J. M., Rubinson, S., Smith, Z., & Rekleitis, I. (2015). Drifter Sensor Network for Environmental Monitoring. 2015 12th Conference on Computer and Robot Vision. doi: 10.1109/crv.2015.10

[27] Xanthidis, M., Li, A. Q., & Rekleitis, I. (2016). Shallow coral reef surveying by inexpensive drifters. OCEANS 2016 - Shanghai. doi: 10.1109/oceansap.2016.7485639